IPN Progress Report 42-242 • August 15, 2025

Realistic and Computationally Efficient 3D Full-Wave Model for Multistatic Scattering from Vegetated Terrains at P/L Band

Ines Fenni[*], **Helene Roussel**[†], **Gaurangi Gupta**[*], **Mehmet Kurum**[‡], **Mohammad Ehsanul Hoque**[‡], **Mark S. Haynes**[*], **Ziad S. Haddad**[*], and **Dylan R. Boyd**[§]

ABSTRACT. — The present article describes the research effort to enhance and validate a computationally efficient 3D full-wave model for electromagnetic (EM) scattering from vegetated terrains at P- and L- frequency bands. The objective is to establish a readily available 3D coherent full-wave model of scattering from realistic complex vegetation scenes that accounts for the vertical and horizontal heterogeneity and, unlike existing scattering models, fully consider wave interactions among vegetation elements and between the vegetation and the soil. Toward this goal, building on a rigorous and coherent forest ultra high frequency (UHF) 3D full-wave model that we have previously developed and validated, we 1) optimize the computational capabilities of the EM numerical solution so that it can efficiently simulate bistatic scattering from realistic large forest or agricultural terrain, 2) improve the vegetated scene representation, and 3) validate the accuracy of the scattering model after enhancements in comparison with the multilevel fast multipole method (MLFMM) implemented in the EM commercial software FEKO.

I. Introduction

Despite the growing interest in remote sensing at the P and L bands of vegetated areas parameters such as soil moisture (SM) [1, 2, 3] and vegetation water content

---

[*] Radar Science and Engineering Section

[†] Sorbonne University, France

[‡] University of Georgia

[§] University of Maryland

The research described in this publication was carried out by the Jet Propulsion Laboratory (JPL), California Institute of Technology, under an internal Research and Technology Development (R&TD) Topic Area project.

(VWC) [4] and the associated efforts made in the last decades to characterize the multistatic electromagnetic (EM) scattering from forest and agricultural terrains at these frequency bands [5, 6, 7, 8, 9], there is still a gap to be filled by accurate 3D coherent models from realistic complex vegetation scenes. This gap is partially a result of the high computational cost of full-wave accurate modeling of EM scattering by arbitrarily shaped and heterogeneous elements, e.g. realistic multispecies trees and crops, rough surface, and layered soil medium. Building on a previous rigorous forest 3D full-wave model, and motivated by the high computational efficiency of a recently enhanced domain decomposition method (DDM) [10, 11, 12], we aim in the present research work to overcome the crippling deficiencies in full-wave models for multistatic scattering from realistic complex forest and agricultural terrains. The key element is the use of a direct solver-based DDM, known as the Characteristic Basis Function Method (CBFM) [13], to overcome the computational efficiency issue that plagues a Method of Moments (MoM)-based full-wave solution. The major advantage of our MoM/CBFM approach is its high accuracy and computational efficiency even when applied to arbitrarily shaped and heterogeneous scatterers. Thus, it enables us to efficiently calculate EM scattering from complex horizontally and vertically heterogeneous scenes, including multispecies vegetation. The ultimate goals of our research effort are to 1) advance our full-wave model in terms of both medium modeling and computational performance, and then 2) use it for the calculation of full-wave EM scattering from electrically large, complex, and heterogeneous realistic vegetation scenes and validate the resulting reflected signals using data from field experiments and NASA's Earth-observing satellites.

In the present progress report, we begin by outlining the motivations behind our scattering model development and its potential applications (Section II). Next, we describe the previous scattering model approach (Section III) then detail our key improvements in two areas: computational efficiency (Section IV) and vegetation medium modeling (Section V). We then validate our enhanced scattering model using the commercial software FEKO, presenting simulation results and performance metrics at P-band, while progressively increasing the dimensions of the simulated vegetation scene (Section VI).

II. Motivations and Applications

Physical scattering models play a leading role in understanding the mechanisms involved in microwave measurements and identifying the vegetated scene features mainly impacting the observed signal. They also enable the study of various forest heterogeneity scenarios under user-defined configurations to conduct uncertainty analysis. Our ability to monitor vegetation dynamics, as vegetation optical depth (VOD), vegetation water content (VWC), and soil mositure (SM), with active and passive data is currently constrained by applying sophisticated EM models rather than it is by technology. Most scattering models represent the VWC as consisting of a homogeneous cloud of water droplets, discarding tree structure and variations in water content as in Figures 1 (a) and (b). These simplifications may result in errors in retrieving VWC or interpreting VOD measurements. More sophisticated EM models, as in Figures 1 (c) and (d), require detailed information about forest architecture. Recent progress in light detection and ranging (LiDAR)-derived vegetation structure may potentially assist in providing such information. However, enhancing the realism and fidelity of the forest scene only makes sense if we develop and use sophisticated and computationally efficient numerical methods to calculate full-wave EM scattering from arbitrarily-shaped and heterogeneous objects.

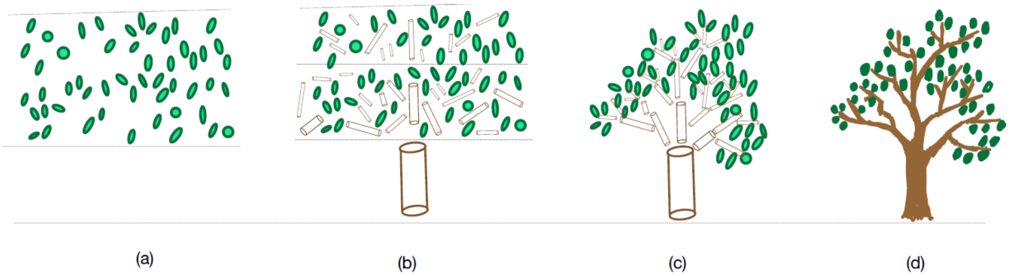

Figure 1. Illustration of tree implementations at different degrees of "photo" realism: (a) dielectric mixing model representation: no scattering, leaves only [14], (b) typical distorted born approximation (DBA) representation: homogeneous, canonical scatters, single scattering [15], (c) enhanced DBA representation: actual architecture, canonical scatters, single scattering [16], (d) the photo-realistic architecture of the full-wave solution: actual architecture, actual constituents [12], [17]. Our research involving the enhancement of a full-wave EM model pertains to category (d).

Our model, involving realistic 3D representation of both vegetation and ground, and full-wave accurate, and computationally efficient EM solver, will provide a clearer understanding of the impact of the complex features of a vegetated scene, including vegetation and soil, on the scattered EM signals, which will help to make the best use of collected microwave land surface measurements. Therefore, we believe that our model will significantly leverage several ongoing and future JPL technologies and research efforts:

- P-band Signals of Opportunity (SoOp) reflectometry has been recently investigated as a viable and cost-effective alternative for remote sensing of Root Zone Soil Moisture (RZSM) under canopy and Snow Water Equivalent (SWE). The basic concept being, instead of installing new radar instruments operating at this highly occupied frequency band, existing telecommunications signals are used as signal sources for P-band SoOp measurements, thereby taking advantage of the P-band's capability to penetrate through vegetation and soil, without bearing the associated cost and frequency allocation problems. Recognizing the potential of this emerging P-band soil moisture (SM) and snow-sensing technology, JPL is currently funding 1) SNOOPI, the first demonstration and validation of the P-band (240-380 MHz) SoOp technique from orbit, and 2) SoOpSAR a new technique for high-resolution remote sensing of snow and soil moisture, combining Synthetic Aperture Radar (SAR) with P-band SoOp techniques. In order to be useful, both technologies require the development of a scattering model that fully captures the interactions between the signal and both the vegetation and the soil, particularly with the wave penetration achieved at P band. Such a model will provide a better representation of the effect of the vegetation and soil properties on the scattered signal, which in turn will enable the development of accurate retrieval algorithms.

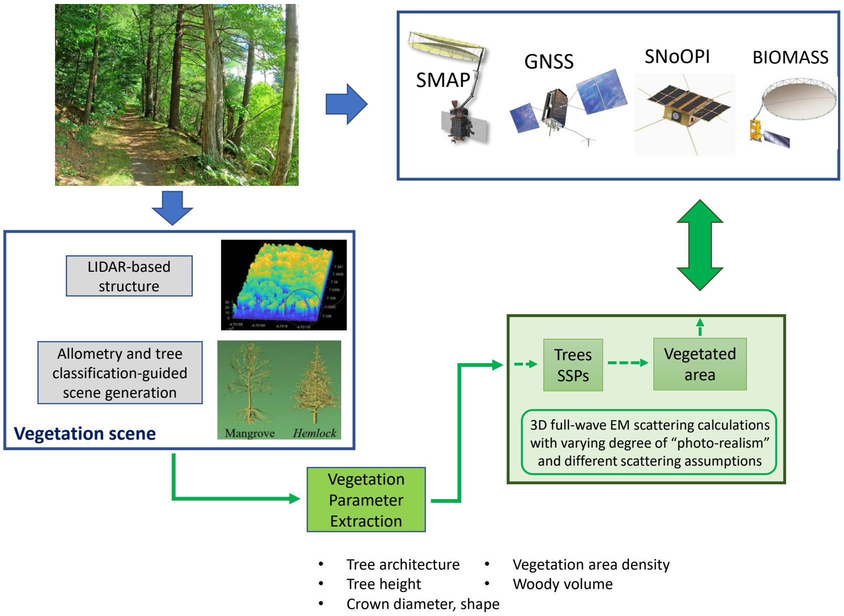

Figure 2. The vegetation parameter extraction and the EM scattering modeling, shown in green, constitute our field of action, to determine the impact of the complex features of a vegetated scene on the scattered EM signals, and optimize the agreement between calculated scattering and measurements.

- Wildfire monitoring and prevention has been a growing interest recently at JPL. In this field, satellite capabilities are quickly maturing, and technology is moving insurance and risk management from responding to catastrophic events to proactive risk mitigation. Thus, there will soon be a real need for full-wave heterogeneous scattering models that can capture the impact of the water content of the trees and the ground soil moisture on the scattered signals. Understanding how the vertical and horizontal heterogeneity of the vegetation (for example: wet vs dry trees, soil moisture) impact the scattering mechanisms and the radar measurements will help improve the fidelity of wildfire models, and their capabilities in terms of estimation and retrieval of forest fuel load from radar remote sensing.

- The European Space Agency (ESA) forest satellite mission BIOMASS will be deployed soon to provide P-band SAR measurements to quantify and track the biomass and carbon stored in forests. The research efforts and new technologies that will walk in the footsteps or draw inspiration from this mission, to quantify the biomass or vegetation optical depth, will need a 3D full-wave model of multistatic scattering from the forest medium at P-band to take full advantage of the data collected by this mission.

- If extended to L-band, there would be potential synergy with NASA missions such as the NASA-ISRO SAR Mission (NISAR), which will operate using L-band SAR to provide detailed Earth observations. Additionally, future missions like the NASA's Surface Topography and Vegetation (STV), although still in the early planning stages, are expected to utilize either L-band SAR, P-band SAR, or both, further enhancing opportunities for collaboration. Aligning with these missions could significantly expand data sources and strengthen scientific outcomes. This synergy ensures greater consistency and complementarity across different remote sensing platforms.

In summary, once the model is implemented and validated, we can produce a reference set of simulations for the numerous relevant NASA calls and ongoing JPL projects, including the L-band NISAR or future missions as it is the case with NASA's STV study, which can culminate in future instruments, likely to utilize either L- or P-band SAR, or both.

Figure 2 summarizes how our 3D full-wave scattering model can be integrated to the forward model workflow and be used through comparisons between its outputs and microwave measurements to study the impact of vegetation parameters and structure on scattered signals. In the present work, vegetation structure refers to the geometry of trees, including their trunks and branches, their orientation, and their spatial distribution. A better understanding of the contribution of the main components of a vegetation scene to the measured scattered signals at P- and L-bands will inform us on the accuracy and legitimacy of many approximations and simplifications commonly used in vegetation forward models. This will inherently contribute to improving the accuracy of retrieval algorithms. To achieve this goal, we will build, as detailed in the remainder of this report, on our advanced capabilities in 1) calculating at a reasonable computational cost the full-wave EM scattering by realistic complex-structured vegetation, and 2) modeling realistic tree structures from LiDAR data.

III. Previous Work

A 3D full-wave model for bistatic scattering from vegetation has been previously developed by co-author Prof. Roussel's research team (including first author Fenni) at Sorbonne University. Based on the volumetric integral equation (VIE) method, this model aims to fully describe the bistatic scattering mechanisms in a forest medium at very high frequency (VHF) / ultra high frequency (UHF) bands [10, 18, 19, 12, 20]. As shown in Figure 3, the trees are described by dielectric vertical and tilted square prisms (in a way to discretize it by cubic cells), representing trunks and main branches, respectively. The trees are placed over a horizontal plane separating two semi-infinite homogeneous media, which are the air and the forest ground. The effects of leaves, needles, and the roughness of the soil are ignored at P-band, since these elements, smaller than the wavelength, contribute only weakly to the scattered field. In order to rigorously characterize the interactions of the vegetation with a plane wave of arbitrary polarization, the 3-D full-wave model is based on the volumetric integral equation method (VIEM) representation of the electric field by using the dyadic Green's function of a two-layered medium [19, 21].

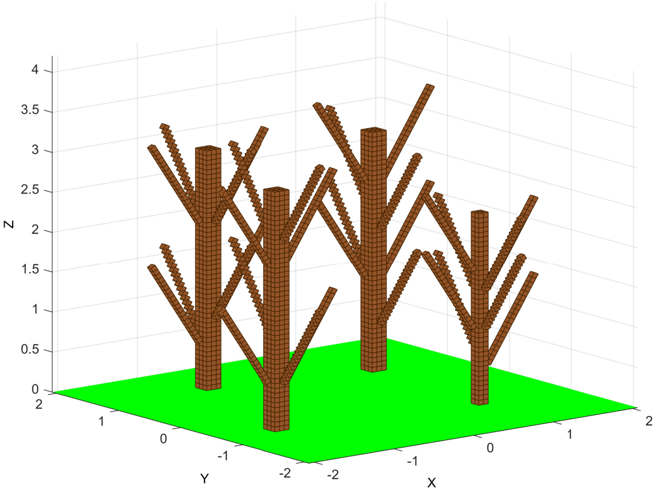

Figure 3. Representative example of forest patch composed of 36 square prisms modeling 4 trees with 8 branches each, placed over a ground plane of relative permittivity $\epsilon_g = 5 + 2.1j$.

The formulation considered here is based on the electric-field integral representation whose kernel is the Green's function of a two-layered medium [11, 10, 22, 23]. The total field $\overrightarrow{E}^t$ at any point $\overrightarrow{r}$ is composed of the reference $\overrightarrow{E}^{ref}$ and scattered $\overrightarrow{E}^s$ fields:

$$\overrightarrow{E}^t(\overrightarrow{r}) = \overrightarrow{E}^{ref}(\overrightarrow{r}) + \overrightarrow{E}^s(\overrightarrow{r}) \tag{1}$$

The reference field $\overrightarrow{E}^{ref}(\overrightarrow{r})$ is the field present when the trees are removed and is the coherent summation of the incident field, $\overrightarrow{E}^{inc}(\overrightarrow{r})$, and the field reflected from the ground, $\overrightarrow{E}^{refl}(\overrightarrow{r})$,

$$\overrightarrow{E}^{ref}(\overrightarrow{r}) = \overrightarrow{E}^{inc}(\overrightarrow{r}) + \overrightarrow{E}^{refl}(\overrightarrow{r}) \tag{2}$$

The scattered field, $\overrightarrow{E}^s(\overrightarrow{r})$, is due to the trees occupying a domain Ω made up of the trunks and branches, and is related to the internal field inside Ω, noted $\overrightarrow{E}^t(\overrightarrow{r}')$.

$$\overrightarrow{E}^s(\overrightarrow{r}) = [\nabla\nabla. + k_1^2]\int_\Omega \chi(\overrightarrow{r}')\overline{\overline{\mathrm{G}}}(\overrightarrow{r},\overrightarrow{r}')\overrightarrow{E}^{\mathrm{t}}(\overrightarrow{r}')\mathrm{d}\overrightarrow{r}' \tag{3}$$

Here, $\chi(\overrightarrow{r}')=\frac{\epsilon(\overrightarrow{r}')-\epsilon_0}{\epsilon_0}$ is the permittivity contrast at the location $\overrightarrow{r'} \in \Omega$, k_1 is the wavenumber in air, and $\overline{\overline{G}}(\overrightarrow{r},\overrightarrow{r}')$ is the dyadic Green's function of two-layered stratified media. By using Eq. 3, we re-write Eq. 1 as:

$$\overrightarrow{E}^t(\overrightarrow{r}) - [\nabla\nabla. + k_1^2]\int_\Omega \chi(\overrightarrow{r}')\overline{\overline{\mathrm{G}}}(\overrightarrow{r},\overrightarrow{r}')\overrightarrow{E}^{\mathrm{t}}(\overrightarrow{r}')\mathrm{d}\overrightarrow{r}' = \overrightarrow{E}^{\mathrm{ref}}(\overrightarrow{r}) \tag{4}$$

To compute $\overrightarrow{E}^t(\overrightarrow{r})$ as expressed in Eq. 1, we first have to determine the total fields inside the trees, namely $\overrightarrow{E}^t(\overrightarrow{r}')$ in Ω, by solving Eq. (4) when $\overrightarrow{r} \in \Omega$. Once $\overrightarrow{E}^t(\overrightarrow{r}')$ in Ω is determined, $\overrightarrow{E}^s$ at all points $\overrightarrow{r}$ above the ground interface could be calculated using Eq. (3).

To determine the total fields inside the trees, the solution of Eq. (4) is performed by means of a Method of Moment (MoM) [24] as follows: the trees are discretized into elementary cubic cells small enough to consider that the field inside each cell is constant. The cell size is equal to or smaller than $\lambda_s/10$, where λ_s is the wavelength inside the scatterers (see Appendix I). Then Eq. (4) reduces to a system of $3N$ linear equations given by:

$$\sum_{q=1}^{3}\sum_{n=1}^{N}(\delta_{mn}\delta_{pq} - \overline{\overline{I}}_{pq}^{mn})\overrightarrow{E}_q^t(\overrightarrow{r}_n) = \overrightarrow{E}_p^{ref}(\overrightarrow{r}_m) \tag{5}$$

where

$$m, n = [1...N] \qquad ; \qquad p, q = [1...3]$$

$$\delta_{mn} = 1 \quad if \quad m = n \quad else \quad \delta_{mn} = 0$$

$$\delta_{pq} = 1 \quad if \quad p = q \quad else \quad \delta_{pq} = 0$$

$$\overline{\overline{I}}_{pq}^{mn} = [\nabla\nabla. + k_1^2]\chi(\overrightarrow{r}_n)\int_{V_{\mathrm{cell}}} \overline{\overline{\mathrm{G}}}_{\mathrm{pq}}(\overrightarrow{r}_{\mathrm{m}}, \overrightarrow{r}'_{\mathrm{n}})\mathrm{d}\overrightarrow{r}'_{\mathrm{n}}$$

Note that q and p are the three components x, y, or z of the fields, N is the total number of mesh elements, m and n are respectively the indices of an observation and source cells, as well as $\overrightarrow{r}_m$ and $\overrightarrow{r}_n$, are respectively the coordinates of the centers of cells m and n. Once the elements of the interaction square matrix and the reference field vector are calculated, the unknown internal field inside the dielectric cells $\overrightarrow{E}_q^t(\overrightarrow{r}_n)$ can be found by solving Eq. (5).

As stated earlier, the next step is to calculate the scattered fields by using Eq. (3) when $\overrightarrow{r}_m$ is the location of the observation point (position of the receiving antenna):

$$\begin{aligned}\overrightarrow{E}_p^s(\overrightarrow{r}_m) = {} & [\nabla\nabla. + k_1^2]\times \\ & \sum_{q=1}^{3}\sum_{n=1}^{N}\chi(\overrightarrow{r}_n)\overrightarrow{E}_q^t(\overrightarrow{r}_n)\int_{V_{\mathrm{cell}}} \overline{\overline{\mathrm{G}}}_{\mathrm{pq}}(\overrightarrow{r}_{\mathrm{m}}, \overrightarrow{r}'_{\mathrm{n}})\mathrm{d}\overrightarrow{r}'_{\mathrm{n}}\end{aligned} \tag{6}$$

In order to increase the capability of this VIEM/MoM model to run electrically large forest scenes by overcoming the limitations introduced by the large number of unknowns and high associated computational cost of the MoM ($O(N^3)$ in CPU time and $O(N^2)$ in memory), an extended CBFM (CBFM-E) compression scheme has been implemented [12, 20]. As a computationally efficient DDM, the basic idea of the CBFM [13, 25, 26, 27, 28] is to replace the numerically large global EM problem with smaller, manageable, and independent local problems, while using appropriate coupling conditions between sub-domains to maintain the accuracy of the solution.

The particular feature that distinguish the CBFM from other DDMs is its use of a direct solver to calculate the unknown electric field inside the global domain. The CBFM operates by generating a new set of basis functions for each sub-domain in order to reduce as much as possible the overall numerical size of the EM problem (by compressing Z^{MoM} so that a direct solver, better adapted for multiple excitation problems, can be used to solve the resulting compressed system of linear equations). The CBFM is thus much better adapted to the calculation of multi-static, multi-excitation scattering problems, because the system of linear equations needs to be solved only once for all considered incident directions. The numerical algorithm of the CBFM is discussed in detail in the next section, specifically the recent enhancement of the computational efficiency of our 3D full-wave MoM/CBFM-based model.

Our 3D full-wave computationally efficient model has been proven accurate when simulated scattered fields are compared to those obtained through a set of indoor (anechoic chamber) bistatic scaled-model measurements [29]. By virtue of the versatility of the MoM/CBFM approach, its applicability to a non-uniform mesh [30] adapted to the heterogeneity of the forest scene and trees, and the high computational efficiency of the CBFM, this first version of the full-wave model has been already used to calculate EM scattering from large heterogeneous forest scenes. For example, with a Message Passing Interface (MPI)-parallelized version [31], the scattered field from a forest scene of 30 m x 30 m, composed of 60 trees and discretized into $N = 406,675$ cells (1,220,025 unknowns), is calculated in only 81 minutes, for a bistatic configuration defined with $\theta_i = \phi_i = 45^o$, $\theta_s = [1:5:90]^o$, and $\phi_s = [1:5:360]^o$, where θ is the zenith angle measured down from the vertical axis z, ϕ is the azimuth measured around z, and (θ_i, ϕ_i) and (θ_s, ϕ_s) describe the incident and scattered wave directions, respectively. With a MoM only-based code (without application of the CBFM), such simulation is just unfeasible with similar computational resources.

The 3D forest model was also used for the analysis of the main scattering mechanisms in forested areas in [19] and, as can be seen in Figure 4, for predicting the scattering characteristics of a complex metallic target located inside a large forested area, in the context of a Foliage Penetration (FoPen) application in [32].

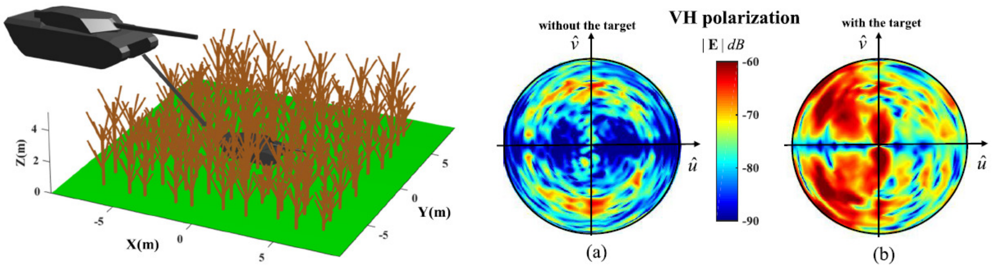

Figure 4. Influence of the presence of a metallic target in a forest environment on the amplitude of the cross-polar VH for an incident direction ($\theta_i = 45^o; \phi_i = 0^o$) [32].

In the remainder of this progress report, we will describe the recent efforts to enhance the computational performance and the vegetation scene realism for this MoM/CBFM based scattering model.

IV. Optimization of the Scattering Model Computational Efficiency

The major contributor to the numerical efficiency of this vegetation scattering model is the implementation of a novel computationally efficient method known as the CBFM [13, 25, 33, 26, 27]. The CBFM is a direct solver-based domain-decomposition algorithm applied to the VIEM/MoM solution to efficiently compute multi-excitation EM scattering from electrically and numerically large arbitrarily shaped and heterogeneous scatterers. The CBFM divides any 3D complex geometry into M blocks, such that the MoM matrix for each block is manageable in size and, thus, can be handled by a direct solver. A set of Macro domain Basis Functions (MBFs) is defined on each block after illuminating it by a sufficient number of incident plane waves [33]. Next, Singular Value Decomposition (SVD) is applied to the MBFs to down-select the number of basis functions and remove potential redundancy introduced by the large number of incident waves. Using the new set of S_i characteristic basis functions (CBFs) for each block i, a final reduced linear set of equations is constructed. The final compressed matrix, of size KK where $K = \sum_{i=1}^{M} S_i$, named Z^c, is generated by applying Galerkin's method to the original matrix Z^{MoM} using the CBFs as both as basis and testing functions [12, 27]. This results in a substantial size-reduction of the initial MoM matrix that is measured by the compression rate CR, which is defined as the ratio between the original number of basis functions in the x, y, and z directions and the number of post-CBFM unknowns: $CR = 3N/K$. Figure 5 summarizes the main steps of the CBFM algorithm. By storing and solving the compressed matrix (Z^c), instead of the original one (Z^{MoM}), we achieve a significant gain in computation time and memory. The higher CR, the smaller the size of the compressed system of linear equations $Z^c\alpha = E^{inc}$, resulting in a better handling of a large number of incident excitations. The CBFM is thus intrinsically better adapted to bistatic scattering configurations, such as SoOp reflectometry, than other iterative solver-based fast numerical techniques such as the Fast Multipole Method (FMM) or Adaptive Cross Approximation (ACA) algorithm.

We recently made significant strides in optimizing the computational performance of the MoM/CBFM solution, in the context of the development of a 3D full-wave model [34, 35] for EM scattering from electrically large precipitation particles. Enhancements mainly include enhanced MPI parallelization of the CBFM and informed sparsification of local MoM matrices and compressed matrix Z^c in order to allow the use of highly efficient parallel direct sparse solvers such as the oneMKL PARDISO. It is worth noting that MPI is a standardized protocol for parallel computing on distributed-memory systems, enabling processes to communicate via explicit message passing. We named this computationally efficient free-space version MIDAS, for MoM Integral-equation Decomposition for Arbitrarily shaped Scatterers, and we validated

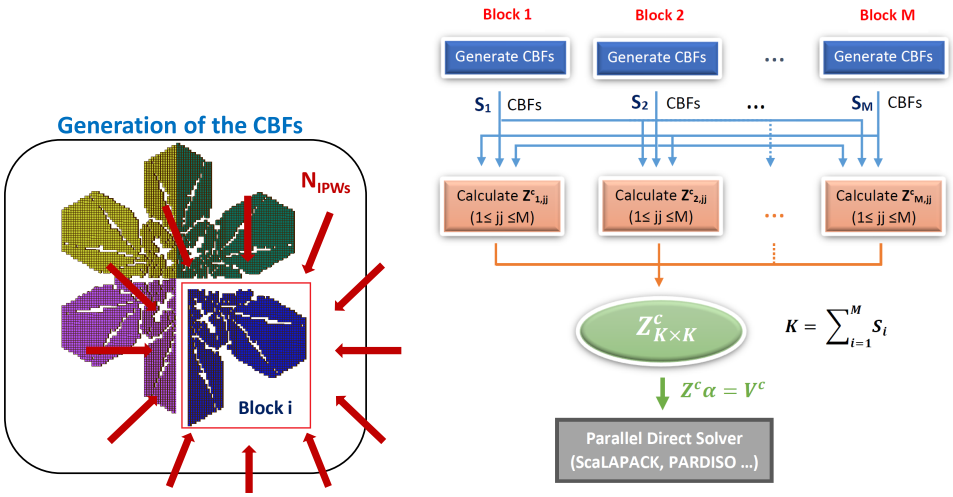

Figure 5. Summary of the Characteristic Basis Function Method (CBFM) algorithm when applied to an example of a realistic arbitrarily-shaped scatterer. CBFs refer to the new reduced set of basis functions, namely the Characteristic Basis Functions.

its accuracy and computational efficiency by comparing the scattering properties of ice, both pristine and aggregates, to the results derived with open-source Discrete Dipole Approximation (DDA) codes [34, 35]. With MIDAS, we have calculated, in less than 20 hours, the scattering matrix of a dense and electrically large Chebyshev particle (16λ in each dimension), discretized into 8,426,060 cells (25 millions unknowns) for a large number of incident waves and scattering directions ($\theta_i = \theta_s = [0:5:180]^o$ and $\phi_i = \phi_s = [0:5:360]^o$). The simulation was performed on the Texas Advanced Computing Center (TACC) supercomputer Stampede2 and used 60 SKX Compute Nodes (48 cores and 192 GB of RAM each) distributed across 360 MPI tasks. Figure 6 describes the computational performance of the code for this simulation in terms of both CPU time and memory usage.

These results demonstrate the potential for the CBFM to simulate electrically large and complex realistic forest scenes. If problems involving tens of million of cells can be achieved, we will be able to provide, at a reasonable computational cost, an accurate 3D full-wave multistatic solution at P band of realistic forest scenes of up to 15m x 15m with a soil depth going up to 1.5 m.

The high computational efficiency of MIDAS spurred us to integrate the performed numerical enhancement techniques into the previous vegetation model described in the previous section. The thus updated model is now called MIDAS-VEG, and we validated its accuracy by comparing its outputs to the EM software FEKO, as detailed later in this progress report. Given the high amenability of the CBFM to parallelization and optimization, we are considering implementing further enhancements, mainly including 1) the efficient MPI parallelization of the multilevel

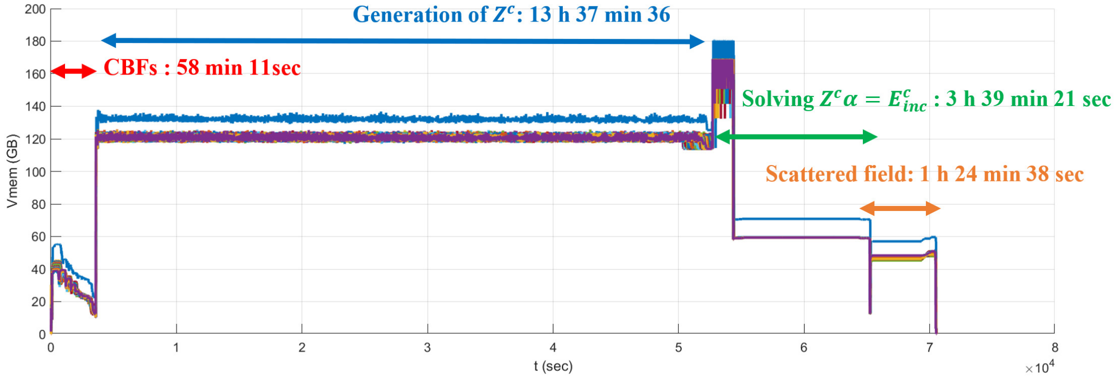

Figure 6. Variations of virtual memory (GB) as function of time for the calculation on 60 SKX nodes (each plot color represents a node) of the EM scattering by a Chebyshev particle of size $16\,\lambda \times 16\,\lambda \times 16\,\lambda$ composed of $Nbc = 8,426,060$ cells for 2701 incident and 2701 scattering directions ($7,295,401$ total combinations). The size of the compressed matrix Z^c is $435,471$ (1.72 $\%$ of the initial MoM matrix)

CBFM [33, 36], particularly adequate to the structure of a vegetation scene where EM interactions among the trees are expected to be weaker than those inside each tree, and 2) the implementation of a mixed resolution mesh [30] adapted to the dielectric properties of the tree components to adequately account for the moisture of different vegetation element while maintaining a manageable numerical size of the vegetation scene.

V. LiDAR-Derived Enhancement of Vegetation Medium Modeling

In this section, we focus on enhancing the realism of the modeled vegetation scene, performed through an ongoing collaboration with co-authors from University of Georgia, who developed advanced capabilities in constructing realistic vegetation structures from LiDAR data [37, 38].

Indeed, increased availability of consumer computing equipment has enabled the development of realistic complex trees and forest characterization over the last three decades [39]. The use of point cloud data has been significantly useful in establishing quantitative structure models (QSM) for trees and forests. QSMs represent the topological structure of trees using basic geometric objects such as cylinders, and thus enable the reconstruction of tree architecture from raw LiDAR scans [40]. The LiDAR scans produce point clouds data, that can be processed with QSMs to create detailed tree architectures described by cylinders. These architectures are simplified based on the requirements of the simulation, thus representing tree implementations at different degrees of “photo-realism”. It is worth noting that, in our study of scattering by realistic vegetation, we make a clear distinction between “photo-realism” and “radio-realism”. Indeed, we define the “radio-realism” as the degree of detail of the vegetation that an EM wave actually sees at the simulation frequency. We can use

LiDAR-based vegetation to determine the "radio-realism" by calculating the 3D full-wave EM scattering of the reconstructed vegetation while decreasing "photo-realism". This allows us to assess what realistic complex features and properties of trees are not actually needed to achieve "radio-realism" at each frequency of interest, namely P- and L-bands.

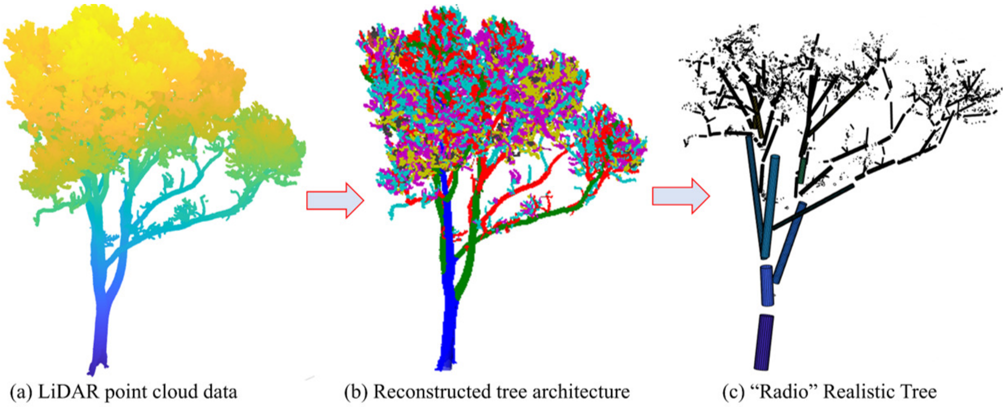
(a) LiDAR point cloud data (b) Reconstructed tree architecture (c) "Radio" Realistic Tree

Figure 7. Example of a reconstructed tree from LiDAR data (a) LiDAR point cloud data ("photo-realistic" representation), (b) tree quantitative structure models (TreeQSM) reconstruction, and (c) simplified cylinder-based reconstruction, that will be examined/verified for "radio-realism".

Figure 7 illustrates the process of reconstructing and simplifying a tree structure from a terrestrial LiDAR scan. Various QSM methods have been open-sourced in the literature; we will use the TreeQSM library [41, 42]. TreeQSM is a method used to reconstruct the woody structure of trees through 3D QSMs. By analyzing terrestrial laser scanning (TLS) data, TreeQSM segments the point cloud into small patches and fits cylinders to these segments. This approach estimates tree parameters such as branch length, diameter, volume, and branching order, providing an accurate representation of tree architecture. Knowing that the detail in the tree architecture affects how different frequencies interact with tree components, we will investigate "radio-realism" at P- and L-bands, by reducing the degree of structure detail through simplifying QSM models, which we refer to in this study as simple cylinder model (SCM). The SCM streamlines the representation of tree architecture by reducing the complexity of the TreeQSM output, through merging consecutive cylinders that share similar characteristics, thereby reducing the total number of cylinders while preserving the tree's essential geometric properties as shown in Figure 7(c).

A last step of voxelization, namely discretization of the geometry into elementary cubic cells, is required to adapt both the reconstructed "photo-realistic" and simplified geometries to MIDAS and MIDAS-VEG. The voxelization process, applied to both QSM and SCM outputs, involves mainly 3 steps: initializing the voxel grid, determining spatial limits, and iteratively checking each cylinder's presence within the voxel grid. In summary, the processing of LiDAR data will be performed in multiple stages as depicted in Figure 8. Raw LiDAR data will be converted into a cylindrical representation through TreeQSM's fitting of small cylinders over patches of point cloud data. Cylinders are then simplified from TreeQSM by replacing cylinders within close proximity to one another within a user-provided angle threshold between unit vectors. To convert from cylinders to voxels, the processes of Figure 8(b-c) are performed, wherein a bounding box discretized to the desired voxel size (depending on the frequency) is created about a cylinder in the simulation coordinate system. The point is considered inside the cylinder based on the projection of the unit vector to the radial axis of the considered cylinder. Passing this check will add a voxel to the final representation of the tree. The resulting voxelized QSM and SCM geometries are then saved as geometry files for import to our EM scattering models MIDAS and MIDAS-VEG.

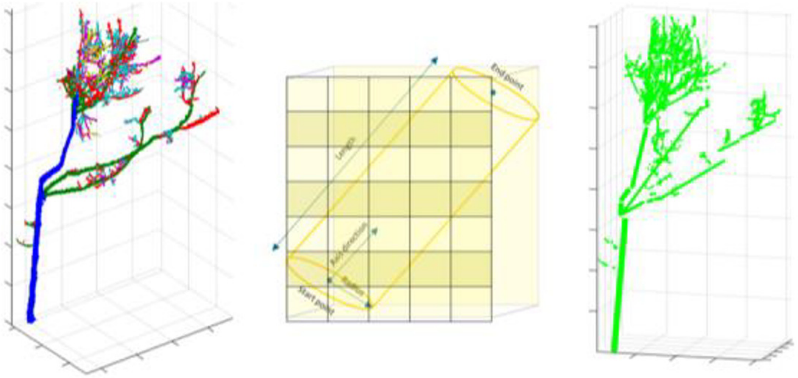

(a) QSM / Cylinders (b) Voxelization (c) Voxel Output

Figure 8. (a) Quantitative structure models (QSM) / simple cylinder model (SCM) reconstructions from terrestrial laser scanning (TLS), (b) illustration of the voxelization approach, (c) final voxelized tree structure ready for input to EM model.

VI. Simulations of EM Scattering by Vegetation at P Band : Results and Validation

Before discussing the validation and computational performance of MIDAS-VEG when used to calculate multistatic scattering by vegetation scenes, we deem it interesting to report on the use of MIDAS [35], the free-space version of our MoM/CBFM solution, to calculate the single scattering properties (SSPs) of realistic LiDAR-based complex-shaped trees. The goal is to leverage the computational efficiency and versatility (to the geometry of the scatterer) of our full-wave model to determine the "radio-realism" at P- and L-bands, as depicted in the previous section. Figure 9 shows an example of the SSPs comparative study. It examines the impact of reducing the tree shape complexity, by applying the SCM to the LiDAR-derived QSM output geometry (left side), on the variations of the extinction and backscattering efficiency factors as a function of incident direction (middle and right columns, respectively). The extinction and backscattering efficiency factors, $Q_{ext} = C_{ext}/\pi a^2$ and $Q_{bks} = C_{bks}/\pi a^2$, shown in Figure 9 are calculated for 482 different incident directions distributed over the sphere surface on spherical design quadrature nodes. C_{ext} and

C_{bks} are the scattering cross sections, and a gives an idea about the density of the tree as it represents the radius of the equivalent-volume sphere with the relation $4/3\pi a^3 = Nd^3$, N being the number of cubic cells composing the tree and d the cell size, namely the discretization resolution determined by the wavelength λ and the real part of the dielectric constant of the scatterer ϵ_r'. d should indeed meet the MoM validity criteria, namely $d \leq \frac{\lambda/\sqrt{\epsilon_r'}}{10}$, to ensure the accuracy of the EM solution.

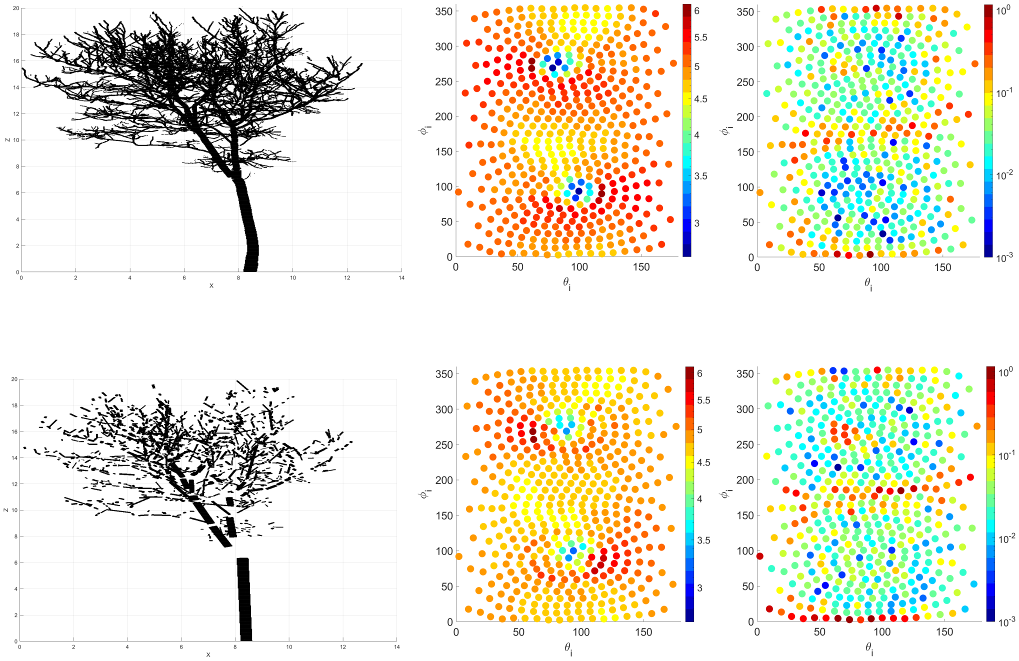

Figure 9. The variations of extinction (middle) and backscattering (right) efficiencies at P-band, as a function of incident direction, for the LiDAR-derived QSM tree shape (top) and its SCM-based simplified version (bottom). The plots show that the simple cylinder model (SCM)-based simplified version has close "radio-realism" to the original LiDAR-derived quantitative structure models (QSM) tree.

The simulated "photo-realistic" tree of Figure 9 has been obtained by applying TreeQSM to TLS data collected at Wytham Woods, Oxfordshire [43] during the winter period of 2015/16 when leaves were off the deciduous trees. At the frequency $f = 300$ MHz and with the dielectric permittivity $\epsilon_r = 9 + i\ 1.2\ e^{-3}$, the QSM-based tree of height $h = 20$ m is voxelized into $N = 616,634$ cells. The scattering matrices are obtained with an MPI-parallelized MIDAS for 482×482 incident/scattering directions combinations in 1 hour 11 minutes, using 4 computing nodes (of 48 CPUs 256 GB each). This initial experiment shows that the scattering matrices obtained for the SCM-based simplified version show significant similarities with the ones obtained for the original LiDAR-derived QSM tree, which suggests that the former has close "radio-realism" to the latter. We record a difference in orientation-averaged (over the total 482 incident directions) backscatter efficiency of 2.27%, with a relative difference per incident direction going up to 80% for a few directions ($\theta_i = 91^o$; $\phi_i = 3.86^o$ for example). We plan to use this experiment set-up to further understand the impact of the vegetation geometry modeling on the scattering properties as a function of the incident direction and simulation frequency, and accordingly improve our SCM algorithm. By virtue of the current MIDAS numerical capabilities, we are able to simulate at P-band (300-450 MHz) a sufficiently large number of realistic trees of various species, heights, shapes, and dielectric compositions at a reasonable amount of time.

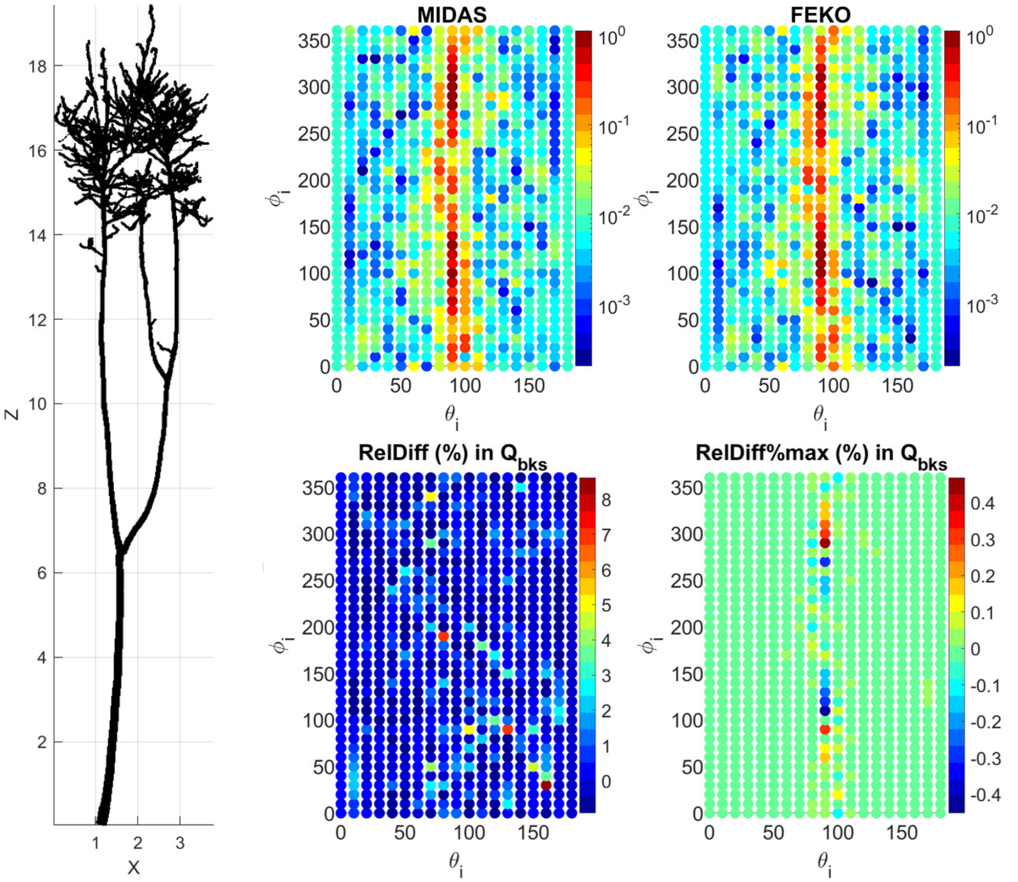

Figure 10. Relative difference (%) in backscattering efficiency factors calculated with MIDAS and FEKO for a LiDAR-derived realistic Wytham winter tree.

We validated the accuracy of the free-space solution MIDAS when applied to the calculation of SPPs of arbitrarily shaped trees by comparing the resulting backscattering efficiency factors Q_{bks} to those obtained with FEKO. Figure 10 plots a comparison in Q_{bks} between MIDAS and FEKO, calculated in a monostatic configuration for 703 incident directions with a uniform step of 10^o in θ and ϕ over the sphere surface. To compare MIDAS and FEKO results, we use the relative difference (Figure 10 bottom middle) defined as $E_r(\theta_{s,i}) = (Q_{bks,MIDAS}(\theta_{s,i}) - Q_{bks,FEKO}(\theta_{s,i}))/Q_{bks,FEKO}(\theta_{s,i})$ and the relative difference compared to the maximum amplitude (Figure 10 bottom right) defined as $E_{r,max}(\theta_{s,i}) = (Q_{bks,MIDAS}(\theta_{s,i}) - Q_{bks,FEKO}(\theta_{s,i}))/max(Q_{bks,FEKO})$. As can be seen in Figure 9, we observe a satisfactory agreement between MIDAS and FEKO with MIDAS being significantly more computationally efficient than FEKO. For MIDAS, with a tree geometry discretized into 95,325 cells and decomposed into 52 CBFM blocks, the calculation of the tree SSPs takes 18 minutes 23 seconds, using 32 parallel MPI tasks on a 64 CPUs/450 GB of RAM computing node of the JPL cluster Gattaca2. When running on a 766 GB RAM local station in a serial mode, FEKO re-meshes the tree geometry imported as stereo-lithography (STL) file into 328,840 dielectric triangles, and takes, using the Multilevel Fast Multipole Method (MLFMM), a total time of 29.951 hours, with most of it dedicated to the solution of the system of linear equations ($\approx$ 28 hours).

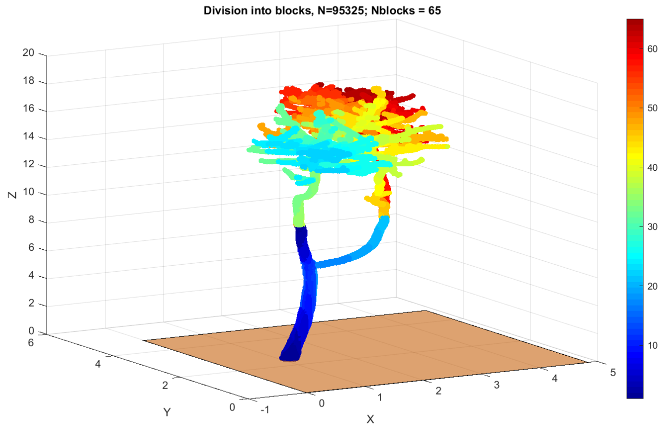

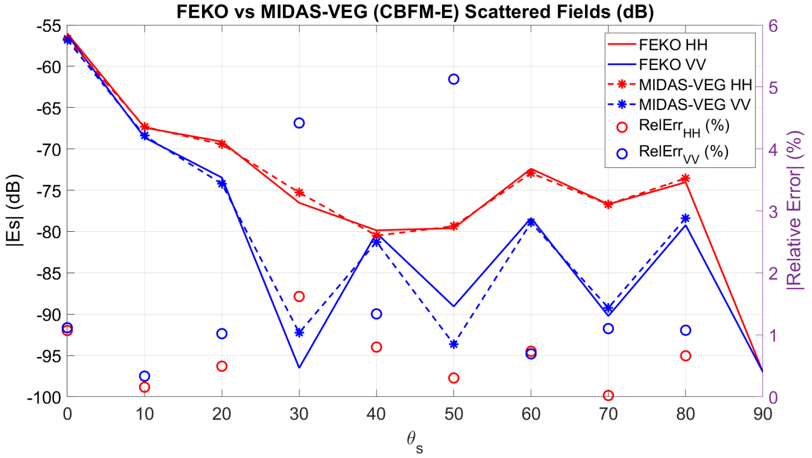

Figure 11. Variations of the magnitude of backscattered fields (VV polarization) computed with the new MIDAS-VEG and FEKO at $f = 2$ GHz for a simple vertical cylinder of dimensions 4 mm x 4 mm x 144 mm posed on a dielectric flat soil ($\epsilon_{soil} = 5 + i3.6$), and a monostatic configuration ($\theta_i = \theta_s = 0 : 10 : 90^o$ and $\phi_i = \phi_s = 0^o$) .

We dedicate the remainder of this section to the assessment of the accuracy and computational performance of MIDAS-VEG in comparison with the EM software FEKO. To validate the integration of MIDAS enhancements into the vegetation model, described in Section IV, we start with reproducing a simple simulation case that has been previously validated in comparison with FEKO in [44]. Figure 11 shows a good agreement between the enhanced MIDAS-VEG and FEKO for the simple case of a vertical cylinder placed on a dielectric plan. As the same configuration has been previously used in [44, 29] to compare the simulation results with measurements performed on reduced-scale models, the height of the cylinder is 144 mm and the simulation frequency is $f = 2$ GHz.

Next, we apply MIDAS-VEG and FEKO to a LiDAR-based tree posed on a dielectric soil to validate the vegetation modeling-related enhancements applied to our scattering model. Figure 11 plots the geometry and division into CBFM blocks of the arbitrarily-shaped tree and the variations of the scattered fields computed with MIDAS and FEKO and the relative error (%) as function of the scattering angle θ_s. We observe again a good agreement between MIDAS and FEKO with a relative error lower than 2% and 5% for HH and VV polarizations, respectively. Relevant computational performance details are provided in Figure 12. MIDAS and FEKO yield comparable results in 1h 27 minutes and approximately 30 hours while running 64 and 16 parallel processes respectively.

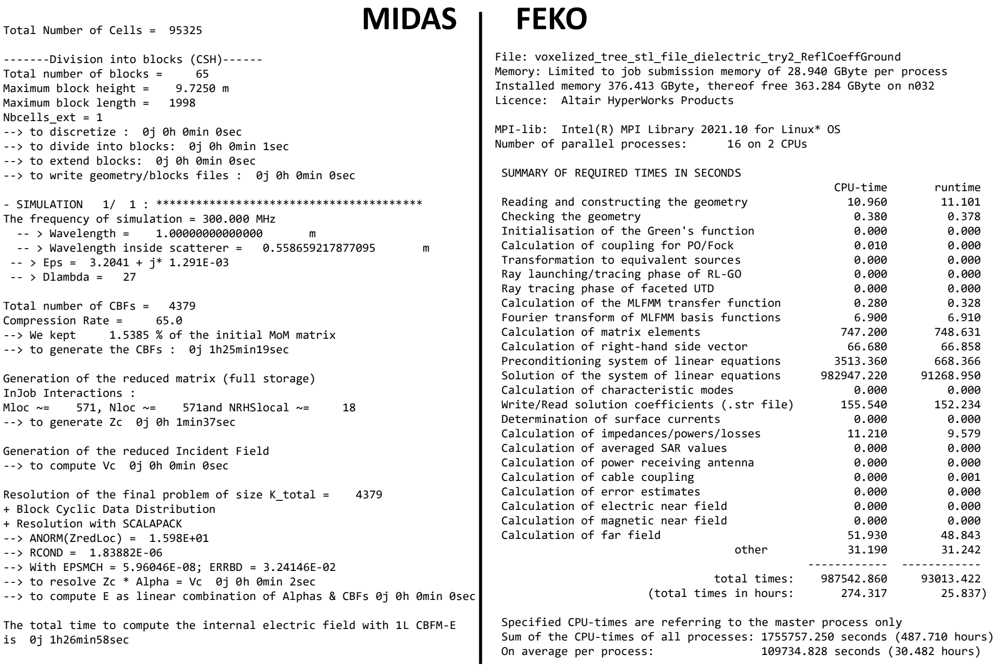

```
Total Number of Cells =  95325

-------Division into blocks (CSH)------
Total number of blocks =     65
Maximum block height =    9.7250 m
Maximum block length =   1998
Nbcells_ext = 1
--> to discretize :  0j 0h 0min 0sec
--> to divide into blocks:  0j 0h 0min 1sec
--> to extend blocks:  0j 0h 0min 0sec
--> to write geometry/blocks files :  0j 0h 0min 0sec

- SIMULATION   1/  1 : ****************************************
The frequency of simulation = 300.000 MHz
  -- > Wavelength =    1.00000000000000       m
  -- > Wavelength inside scatterer =   0.558659217877095       m
 -- > Eps =  3.2041 + j* 1.291E-03
 -- > Dlambda =   27

Total number of CBFs =   4379
Compression Rate =     65.0
--> We kept     1.5385 % of the initial MoM matrix
--> to generate the CBFs :  0j 1h25min19sec

Generation of the reduced matrix (full storage)
InJob Interactions :
Mloc ~=    571, Nloc ~=    571and NRHSlocal ~=     18
--> to generate Zc  0j 0h 1min37sec

Generation of the reduced Incident Field
--> to compute Vc  0j 0h 0min 0sec

Resolution of the final problem of size K_total =    4379
+ Block Cyclic Data Distribution
+ Resolution with SCALAPACK
--> ANORM(ZredLoc) =  1.598E+01
--> RCOND =  1.83882E-06
--> With EPSMCH = 5.96046E-08; ERRBD = 3.24146E-02
--> to resolve Zc * Alpha = Vc  0j 0h 0min 2sec
--> to compute E as linear combination of Alphas & CBFs 0j 0h 0min 0sec

The total time to compute the internal electric field with 1L CBFM-E
is  0j 1h26min58sec
```

```
File: voxelized_tree_stl_file_dielectric_try2_ReflCoeffGround
Memory: Limited to job submission memory of 28.940 GByte per process
Installed memory 376.413 GByte, thereof free 363.284 GByte on n032
Licence:  Altair HyperWorks Products

MPI-lib:  Intel(R) MPI Library 2021.10 for Linux* OS
Number of parallel processes:      16 on 2 CPUs

 SUMMARY OF REQUIRED TIMES IN SECONDS
                                                    CPU-time       runtime
 Reading and constructing the geometry                10.960        11.101
 Checking the geometry                                 0.380         0.378
 Initialisation of the Green's function                0.000         0.000
 Calculation of coupling for PO/Fock                   0.010         0.000
 Transformation to equivalent sources                  0.000         0.000
 Ray launching/tracing phase of RL-GO                  0.000         0.000
 Ray tracing phase of faceted UTD                      0.000         0.000
 Calculation of the MLFMM transfer function            0.280         0.328
 Fourier transform of MLFMM basis functions            6.900         6.910
 Calculation of matrix elements                      747.200       748.631
 Calculation of right-hand side vector                66.680        66.858
 Preconditioning system of linear equations         3513.360       668.366
 Solution of the system of linear equations       982947.220     91268.950
 Calculation of characteristic modes                   0.000         0.000
 Write/Read solution coefficients (.str file)        155.540       152.234
 Determination of surface currents                     0.000         0.000
 Calculation of impedances/powers/losses              11.210         9.579
 Calculation of averaged SAR values                    0.000         0.000
 Calculation of power receiving antenna                0.000         0.000
 Calculation of cable coupling                         0.000         0.001
 Calculation of error estimates                        0.000         0.000
 Calculation of electric near field                    0.000         0.000
 Calculation of magnetic near field                    0.000         0.000
 Calculation of far field                             51.930        48.843
                                      other           31.190        31.242
                                                ------------  ------------
                                total times:      987542.860     93013.422
                       (total times in hours:        274.317        25.837)

 Specified CPU-times are referring to the master process only
 Sum of the CPU-times of all processes: 1755757.250 seconds (487.710 hours)
 On average per process:                109734.828 seconds (30.482 hours)
```

Figure 12. Details of computational performance of MIDAS and FEKO while running the simulation case of Figure 11, extracted from both software output files.

Most recently, we applied MIDAS-VEG to the example of vegetation scene of 45 x 45 m^2 of Figure 13 randomly generated from the set of LiDAR-based voxelized QSM shapefiles of Wytham winter trees [43]. To comply with MoM validity criteria at $f = 300$ GHz, the entire vegetation scene is discretized into $N = 1,506,207$ mesh elements of size $d = 5$ cm. Using 8 JPL Gattaca nodes (64 CPUs, 450 GB of RAM each) as 512 MPI tasks, it took MIDAS 140 minutes 16 seconds to calculate the scattered fields at $N_{Tr} = 90$ different incident directions ($\theta_i = 0 : 10 : 90^o$; $\phi_i = 0 : 45 : 360^o$) with $N_{Rx} = 2275$ scattering directions for each ($\theta_s = 0 : 1 : 90^o$; $\phi_s = 0 : 15 : 360^o$).

We refrain from including plots of the scattered fields at this development stage, as the validation and verification process is still ongoing. We plan to validate MIDAS-VEG accuracy for a multiple trees vegetation scene by comparing results for a simplified scene containing only 2 or 3 trees with FEKO, due to the high computational cost associated with the latter.

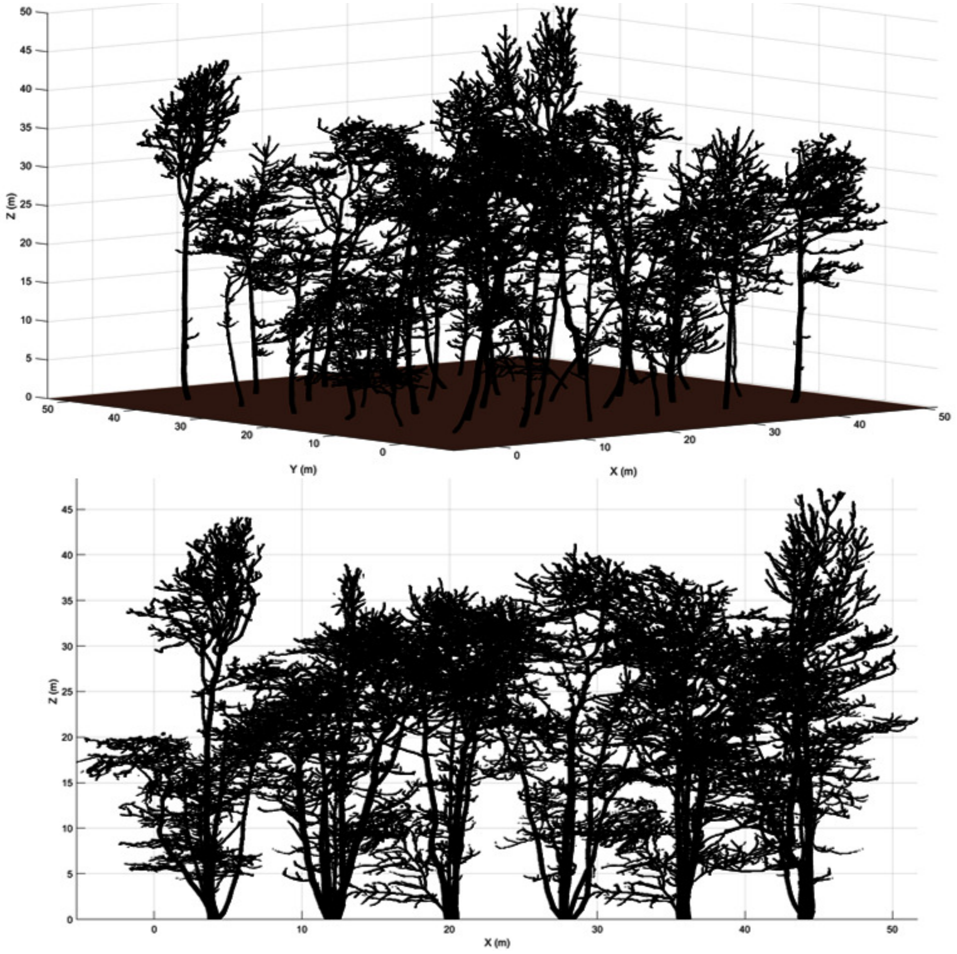

Figure 13. Example of a realistic vegetation scene built using voxelized QSM geometries generated as described in Section V from leaf-off terrestrial laser scanning data of Wytham Woods [43].

VII. Conclusions and Perspectives

We made good progress in enhancing a 3D full-wave model for bistatic scattering from vegetated scenes to make it a highly useful tool for the forward scattering modelers, and soil moisture and vegetation water content retrieval algorithm developers at P and L band. Enhancements include improving the vegetated scene representation in terms of tree geometry and heterogeneity, and optimizing the computational capabilities of the MoM/CBFM solution so that it can efficiently simulate bistatic scattering from a large realistic forest or agricultural terrain.

Next, we plan to augment tree geometry modeling by leveraging prior efforts on tree species definition, classification, and realization (for PolSARProSim+ [45, 46]). We are working on building a vegetation models database from different tree and short vegetation generation tools (LiDAR data, PolSARProSim+). After finalizing validation of the scattering model at P-band, we aim to increase the computational efficiency of the P-band vegetation scattering model to extend its applicability to small forest patches (typically 10m x 10m of vegetation only) to estimate the transmissivity at L band of limited field-of-view sections of the forest. This mainly involves an MPI-optimized careful implementation of the multilevel Characteristic Basis Function Method (ML-CBFM) with appropriate load balancing and parallel resource allocation through the different levels.

Acknowledgments

The research was carried out at the Jet Propulsion Laboratory, California Institute of Technology, under a JPL Research and Technology Development (RTD) Topic area project.

References

[1] J. Garrison, Y.-C. Lin, B. Nold, J. R. Piepmeier, M. A. Vega, M. Fritts, C. F. Du Toit, and J. Knuble, “Remote sensing of soil moisture using P-band signals of opportunity (SoOp): Initial results,” *2017 IEEE International Geoscience and Remote Sensing Symposium (IGARSS), Fort Worth, Texas*, pp. 4158–4161, 2017.

[2] J. L. Garrison, M. Kurum, B. Nold, J. Piepmeier, M. A. Vega, R. Bindlish, and G. Pignotti, “Remote sensing of root-zone soil moisture using I- and P-band signals of opportunity: Instrument validation studies,” *2018 IEEE International Geoscience and Remote Sensing Symposium (IGARSS), Valencia, Spain*, pp. 8305–8308, 2018.

[3] S. H. Yueh, X. Xu, R. Shah, S. Margulis, and K. Elder, “P-band signals of opportunity for remote sensing of root zone soil moisture,” *2018 IEEE International Geoscience and Remote Sensing Symposium (IGARSS), Valencia, Spain*, pp. 1403–1406, 2018.

[4] A. G. Konings, S. S. Saatchi, C. Frankenberg, M. Keller, V. Leshyk, W. R. Anderegg, V. Humphrey, A. M. Matheny, A. Trugman, L. Sack *et al.*, “Detecting forest response to droughts with global observations of vegetation water content,” *Global Change Biology*, vol. 27, no. 23, pp. 6005–6024, 2021.

[5] M. Burgin, D. Clewley, R. M. Lucas, and M. Moghaddam, “A generalized radar backscattering model based on wave theory for multilayer multispecies vegetation,” *IEEE Transactions on Geoscience and Remote Sensing*, vol. 49, no. 12, pp. 4832–4845, 2011.

[6] S.-B. Kim, M. Moghaddam, L. Tsang, M. Burgin, X. Xu, and E. G. Njoku, “Models of L-band radar backscattering coefficients over global terrain for soil moisture retrieval,” *IEEE Transactions on Geoscience and Remote Sensing*, vol. 52, no. 2, pp. 1381–1396, February 2014.

[7] L. Tsang, T.-H. Liao, S. Tan, H. Huang, T. Qiao, and K.-H. Ding, “Rough surface and volume scattering of soil surfaces, ocean surfaces, snow, and vegetation based on numerical Maxwell model of 3-D simulations,” *IEEE Journal of Selected Topics in Applied Earth Observations and Remote Sensing*, vol. 10, no. 11, pp. 4703–4720, 2017.

[8] H. Huang, L. Tsang, E. G. Njoku, A. Colliander, T.-H. Liao, and K.-H. Ding, “Propagation and scattering by a layer of randomly distributed dielectric cylinders using Monte Carlo simulations of 3D Maxwell equations with applications in microwave interactions with vegetation,” *IEEE Access*, vol. 5, pp. 11 985–12 003, 2017.

[9] M. Kurum, M. Deshpande, A. T. Joseph, P. E. O’Neill, R. H. Lang, and O. Eroglu, “SCoBi-Veg: A generalized bistatic scattering model of reflectometry from vegetation for signals of opportunity applications,” *IEEE Transactions on Geoscience and Remote Sensing*, vol. 57, no. 2, pp. 1049–1068, 2019.

[10] H. Nguyen, H. Roussel, and W. Tabbara, “A coherent model of forest scattering and SAR imaging in the VHF and UHF-band,” *IEEE Transactions on Geoscience and Remote Sensing*, vol. 44, no. 4, pp. 838–848, 2006.

[11] S. Bellez, C. Dahon, and H. Roussel, “Integral representation of the electromagnetic field for the description of the main mechanisms appearing in forested area for monostatic radar configurations,” *2008 IEEE International Geoscience and Remote Sensing Symposium (IGARSS), Boston, Massachusetts*, vol. 4, pp. IV – 1113–IV – 1116, July 2008.

[12] I. Fenni, H. Roussel, M. Darces, and R. Mittra, "Fast analysis of large 3-D dielectric scattering problems arising in remote sensing of forest areas using the CBFM," *IEEE Transactions on Antennas and Propagation*, vol. 62, no. 8, pp. 4282–4291, 2014.

[13] R. Mittra and K. Du, "Characteristic basis function method for iteration-free solution of large method of moments problems," *Progress In Electromagnetics Research B*, vol. 6, pp. 307–336, 2008.

[14] V. Humphrey and C. Frankenberg, "Continuous ground monitoring of vegetation optical depth and water content with GPS signals," *Biogeosciences Discussions*, pp. 1–44, 2022.

[15] M. Kurum, M. M. Farhad, and D. Boyd, "GNSS transmissometry (GNSS-T): Modeling propagation of GNSS signals through forest canopy," *2022 IEEE International Geoscience and Remote Sensing Symposium (IGARSS), Kuala Lumpur, Malaysia*, pp. 4695–4698, 2022.

[16] S. Yadav and A. Ghosh, "A realistic framework of GNSS-T for simulating scattering and propagation of GNSS signals under a forest canopy," *PhotonIcs and Electromagnetics Research Symposium*, 2023.

[17] W. Gu, L. Tsang, A. Colliander, and S. Yueh, "Hybrid method for full-wave simulations of forests at L-band," *IEEE Access*, vol. 10, pp. 105 898–105 909, 2022.

[18] Y. Ziade, H. Roussel, M. Lesturgie, and W. Tabbara, "A coherent model of forest propagation— Application to detection and localization of targets using the DORT method," *IEEE Transactions on Antennas and Propagation*, vol. 56, no. 4, pp. 1048–1057, 2008.

[19] S. Bellez, C. Dahon, and H. Roussel, "Analysis of the main scattering mechanisms in forested areas: An integral representation approach for monostatic radar configurations," *IEEE Transactions on Geoscience and Remote Sensing*, vol. 47, no. 12, pp. 4153–4166, 2009.

[20] I. Fenni, H. Roussel, M. Darces, and R. Mittra, "Efficiency enhancement of the characteristic basis function method for modeling forest scattering using the adaptive cross approximation algorithm," *IEEE Transactions on Antennas and Propagation*, vol. 64, no. 10, pp. 4539–4544, 2016.

[21] T.-J. Cui and W. C. Chew, "Fast evaluation of Sommerfeld integrals for EM scattering and radiation by three-dimensional buried objects," *IEEE Transactions on Geoscience and Remote Sensing*, vol. 37, no. 2, pp. 887–900, Mar 1999.

[22] L. Angot, H. Roussel, and W. Tabbara, "A full wave three dimensional analysis of forest remote sensing using VHF electromagnetic wave," *Progress In Electromagnetics Research*, vol. 38, pp. 311–331, 2002.

[23] W. C. Chew, *Waves and Fields in Inhomogenous Media.* Hoboken, New Jersey: Wiley-IEEE Press, 1999.

[24] M. M. Ney, "Method of moments as applied to electromagnetic problems," *IEEE Transactions on Microwave Theory and Techniques*, vol. 33, no. 10, pp. 972–980, 1985.

[25] R. Mittra, V. V. S. Prakash, and J. Yeo, "Some novel techniques for efficient analysis of large arrays and frequency selective radomes," *Twelfth International Conference on Antennas and Propagation, Exeter, United Kingdom, Conf. Publ. No. 491*, vol. 2, pp. 462–465, 2003.

[26] R. Maaskant, "Analysis of large antenna systems," Ph.D. dissertation, Technische Universiteit Eindhoven, 2010.

[27] R. Maaskant, R. Mittra, and A. Tijhuis, “Fast analysis of large antenna arrays using the characteristic basis function method and the adaptive cross approximation algorithm,” *IEEE Transactions on Antennas and Propagation*, vol. 56, no. 11, pp. 3440–3451, Nov 2008.

[28] E. Garcia, C. Delgado, I. G. Diego, and M. F. Catedra, “An iterative solution for electrically large problems combining the characteristic basis function method and the multilevel fast multipole algorithm,” *IEEE Transactions on Antennas and Propagation*, vol. 56, no. 8, pp. 2363–2371, 2008.

[29] S. Bellez, H. Roussel, C. Dahon, J. C. Castelli, and A. Cheraly, “Full polarimetric bistatic radar imaging experiments on sets of dielectric cylinders above a conductive circular plate,” *IEEE Transactions on Geoscience and Remote Sensing*, vol. 51, no. 7, pp. 4164–4176, 2013.

[30] I. Fenni, H. Roussel, M. Darces, and R. Mittra, “Application of the characteristic basis function method (CBFM) on a non-uniform mesh to the solution of large-size dielectric scattering problems,” *The 8th European Conference on Antennas and Propagation (EuCAP 2014),The Hague, The Netherlands*, pp. 2423–2426, 2014.

[31] M. Fall, H. Roussel, C. Dahon, M. Casaletti, I. Fenni, and R. Mittra, “A high performance MPI implementation of numerical modeling of electromagnetic scattering from forest environment,” *2016 IEEE International Symposium on Antennas and Propagation (APSURSI), Fajardo, Puerto Rico*, pp. 2011–2012, 2016.

[32] L. Hettak, H. Roussel, M. Casaletti, C. Dahon, and R. Mittra, “Hybrid formulation for the electromagnetic analysis of metallic objects placed in natural environments,” *2017 11th European Conference on Antennas and Propagation (EUCAP), Paris, France*, pp. 3534–3537, 2017.

[33] J. Laviada, F. Las-Heras, M. R. Pino, and R. Mittra, “Solution of electrically large problems with multilevel characteristic basis functions,” *IEEE Transactions on Antennas and Propagation*, vol. 57, no. 10, pp. 3189–3198, 2009.

[34] I. Fenni, Z. S. Haddad, H. Roussel, K.-S. Kuo, and R. Mittra, “A computationally efficient 3-D full-wave model for coherent EM scattering from complex-geometry hydrometeors based on MoM/CBFM-enhanced algorithm,” *IEEE Transactions on Geoscience and Remote Sensing*, vol. 56, no. 5, pp. 2674–2688, May 2018.

[35] I. Fenni, K.-S. Kuo, M. S. Haynes, Z. S. Haddad, and H. Roussel, “Evaluation of higher-order quadrature schemes in improving computational efficiency for orientation-averaged single-scattering properties of nonspherical ice particles,” *Journal of Geophysical Research: Atmospheres*, vol. 126, no. 11, 2021.

[36] Y. Su, C. Li, R. Mittra, and W. Sheng, “Multi-level characteristic basis function method for analysis of scattering from objects embedded in multi-layered media,” *Journal of Electromagnetic Waves and Applications*, vol. 31, no. 1, pp. 47–56, 2017.

[37] M. E. Hoque and M. Kurum, “GNSS-T forest transmissivity simulations based on LiDAR-derived tree structure,” *2025 United States National Committee of URSI National Radio Science Meeting (USNC-URSI NRSM), Boulder, Colorado*, pp. 324–325.

[38] D. Boyd, M. Kurum, S. Yadav, M. Hoque, A. Ghosh, M. Farhad, I. Fenni, E. Macorps, and B. Osmanoglu, “Exploring the impact of tree structure on forest transmissivity modeling,” *2024 IEEE International Geoscience and Remote Sensing Symposium (IGARSS 2024), Athens, Greece*, pp. 542–546, 2024.

[39] R. J. Hartley, S. Jayathunga, J. Morgenroth, and G. D. Pearse, “Tree branch characterisation from point clouds: A comprehensive review,” *Current Forestry Reports*, vol. 10, no. 5, pp. 360–385, 2024.

[40] J. Hackenberg, C. Morhart, J. Sheppard, H. Spiecker, and M. Disney, “Highly accurate tree models derived from terrestrial laser scan data: A method description,” *Forests*, vol. 5, no. 5, pp. 1069–1105, 2014.

[41] P. Raumonen, M. Kaasalainen, M. Åkerblom, S. Kaasalainen, H. Kaartinen, M. Vastaranta, M. Holopainen, M. Disney, and P. Lewis, “Fast automatic precision tree models from terrestrial laser scanner data,” *Remote Sensing*, vol. 5, no. 2, pp. 491–520, 2013.

[42] A. Lau, L. P. Bentley, C. Martius, A. Shenkin, H. Bartholomeus, P. Raumonen, Y. Malhi, T. Jackson, and M. Herold, “Quantifying branch architecture of tropical trees using terrestrial LiDAR and 3D modelling,” *Trees*, vol. 32, pp. 1219–1231, 2018.

[43] K. Calders, H. Verbeeck, A. Burt, N. Origo, J. Nightingale, Y. Malhi, P. Wilkes, P. Raumonen, R. Bunce, and M. Disney, “Terrestrial laser scanning data Wytham Woods: leaf-off raw data 2015/16,” *NERC EDS Center for Environmental Data Analysis*, 15 November 2022.

[44] S. Bellez, “Contribution à l’analyse de la diffusion bistatique par un milieu forestier dans les bandes VHF et UHF à l’aide d’une représentation intégrale du champ électrique et de mesures en chambres anéchoïques,” Ph.D. dissertation, Université Pierre et Marie Curie, 2010.

[45] S. Hensley, R. Ahmed, B. Chapman, B. Hawkins, M. Lavalle, N. Pinto, M. Pardini, K. Papathanassiou, P. Siqueria, and R. Treuhaft, “A comparison of L-band and S-band interferometry and tomography of the BERMS boreal forest with UAVSAR and F-SAR datasets,” *13th European Conference on Synthetic Aperture Radar (EUSAR 2021).*

[46] S. Hensley, T. Michel, M. Neumann, M. Lavalle, R. Ahmed, R. Muellerschoen, and B. Chapman, “A comparison of multi-baseline polarimetric inteferometry at La Amistad and La Selva, Costa Rica with a modified PolSARProSim scattering tool,” *10th European Conference on Synthetic Aperture Radar (EUSAR 2014), Berlin, Germany*, pp. 1–4, 2014.

APPENDIX

I. Elements of the MoM Matrix

The initial MoM Matrix that represents the interactions between the different cells composing the simulation scene, is of size $3N \times 3N$ where N is the total number of cells. It is written as follows

$$\underline{\mathbf{Z}} = \begin{bmatrix} \begin{bmatrix} \mathrm{Z}^{\mathrm{mn}}_{\mathrm{xx}} \\ \mathrm{Z}^{\mathrm{mn}}_{\mathrm{yx}} \\ \mathrm{Z}^{\mathrm{mn}}_{\mathrm{zx}} \end{bmatrix} & \begin{bmatrix} \mathrm{Z}^{\mathrm{mn}}_{\mathrm{xy}} \\ \mathrm{Z}^{\mathrm{mn}}_{\mathrm{yy}} \\ \mathrm{Z}^{\mathrm{mn}}_{\mathrm{zy}} \end{bmatrix} & \begin{bmatrix} \mathrm{Z}^{\mathrm{mn}}_{\mathrm{xz}} \\ \mathrm{Z}^{\mathrm{mn}}_{\mathrm{yz}} \\ \mathrm{Z}^{\mathrm{mn}}_{\mathrm{zz}} \end{bmatrix} \end{bmatrix} \tag{7}$$

The coefficients $\mathrm{Z}^{\mathrm{mn}}_{\mathrm{pq}}$ of the MoM matrix are expressed as :

$$\mathrm{Z}^{\mathrm{mn}}_{\mathrm{pq}} = \delta_{\mathrm{mn}}\delta_{\mathrm{pq}} - \mathrm{Z}^{\mathrm{s,\,mn}}_{\mathrm{pq}} - \mathrm{Z}^{\mathrm{r,\,mn}}_{\mathrm{pq}} \tag{8}$$

The product $\delta_{mn}\delta_{pq}$ is equal to 1 only for the diagonal elements of the MoM matrix $\underline{\mathbf{Z}}$. δ_{mn} and δ_{pq} are the Kronecker delta functions defined as

$$\delta_{mn},\, \delta_{pq} = \begin{cases} 1 & \text{if} \quad m = n,\, p = q \\ 0 & \text{if} \quad m \neq n,\, p \neq q \end{cases} \tag{9}$$

$$\mathrm{Z}^{\mathrm{s,\,mn}}_{\mathrm{pq}} = \mathrm{k}_0^2 \int_{V_{\mathrm{cell}}} \chi(\overrightarrow{r}'_{\mathrm{n}}) \mathrm{G}^{\mathrm{s}}_{\mathrm{pq}}(\overrightarrow{r}_{\mathrm{m}}, \overrightarrow{r}'_{\mathrm{n}}) \mathrm{d}\overrightarrow{r}'_{\mathrm{n}} + \sum_{\mathrm{q}=1}^{3} \frac{\partial^2}{\partial \mathrm{p_m q_m}} \int_{V_{\mathrm{cell}}} \chi(\overrightarrow{r}'_{\mathrm{n}}) \mathrm{G}^{\mathrm{s}}_{\mathrm{pq}}(\overrightarrow{r}_{\mathrm{m}}, \overrightarrow{r}'_{\mathrm{n}}) \mathrm{d}\overrightarrow{r}'_{\mathrm{n}} \tag{10}$$

$$\mathrm{Z}^{\mathrm{r,\,mn}}_{\mathrm{pq}} = \mathrm{k}_0^2 \int_{V_{\mathrm{cell}}} \chi(\overrightarrow{r}'_{\mathrm{n}}) \mathrm{G}^{\mathrm{r}}_{\mathrm{pq}}(\overrightarrow{r}_{\mathrm{m}}, \overrightarrow{r}'_{\mathrm{n}}) \mathrm{d}\overrightarrow{r}'_{\mathrm{n}} + \sum_{\mathrm{q}=1}^{3} \frac{\partial^2}{\partial \mathrm{p_m q_m}} \int_{V_{\mathrm{cell}}} \chi(\overrightarrow{r}'_{\mathrm{n}}) \mathrm{G}^{\mathrm{r}}_{\mathrm{pq}}(\overrightarrow{r}_{\mathrm{m}}, \overrightarrow{r}'_{\mathrm{n}}) \mathrm{d}\overrightarrow{r}'_{\mathrm{n}} \tag{11}$$

$\overrightarrow{r}_m$ is the coordinate vector of the observation point m; $\overrightarrow{r}'_n$ is the coordinate vector of the center of the source cell n; $p, q = x, y, z$; k_0 is the wavelength number in the air; $\mathrm{G}^{\mathrm{s}}_{\mathrm{pq}}$ is the component pq of the singular dyadic Green's function; $\mathrm{G}^{\mathrm{r}}_{\mathrm{pq}}$ is the component pq of the regular dyadic Green's function; and $\chi(\overrightarrow{r}') = \dfrac{\epsilon(\overrightarrow{r}') - \epsilon_0}{\epsilon_0}$ is the dielectric contrast.

We assume that :

$$\int_{V_{\mathrm{cell}}} \chi(\overrightarrow{r}'_{\mathrm{n}}) \mathrm{G}^{\psi}_{\mathrm{pq}}(\overrightarrow{r}_{\mathrm{m}}, \overrightarrow{r}'_{\mathrm{n}}) \mathrm{d}\overrightarrow{r}'_{\mathrm{n}} = \chi_{\mathrm{n}} \int_{V_{\mathrm{cell}}} \mathrm{G}^{\psi}_{\mathrm{pq}}(\overrightarrow{r}_{\mathrm{m}}, \overrightarrow{r}'_{\mathrm{n}}) \mathrm{d}\overrightarrow{r}'_{\mathrm{n}} \tag{12}$$

where $\psi = \mathrm{s}, \mathrm{r}$. If the domain Ω is homogeneous, the dielectric contrast $\chi(\overrightarrow{r}'_n)$ does not depend on the position $\overrightarrow{r}'_n$ and it is thus equal to $\Delta\epsilon = \epsilon_r - 1$.